Pure and Applied Geophysics

Microstructural Inhomogeneity and Mechanical Anisotropy Associated with Bedding in Rothbach Sandstone

Laurent Louis,[1] Patrick Baud,[2] and Teng-fong Wong[3]

Abstract—This study present the result of conventional triaxial tests conducted on samples of Rothbach sandstone cored parallel, oblique (at 45 degrees) and perpendicular to the bedding at effective pressures ranging from 5 to 250 MPa. Mechanical and microstructural data were used to determine the role of the bedding on mechanical strength and failure mode. We find that samples cored at 45 degrees to the bedding yield at intermediate level of differential stress between the ones for parallel and perpendicular samples at all effective pressures. Strain localization at high confining pressure (i.e., in the compactive domain) is observed in samples perpendicular and oblique to the bedding but not in samples cored parallel to the bedding. However, porosity reduction is comparable whether compactive shear bands, compaction bands or homogeneous cataclastic flow develop. Microstructural data suggest that (1) mechanical anisotropy is controlled by a preferred intergranular contact alignment parallel to the bedding and that (2) localization of compaction is controlled by bedding laminations and grain scale heterogeneity, which both prevent the development of well localized compaction features.

Key words: Sandstone, mechanical strength, anisotropy, strain localization, heterogeneity.

1. Introduction

Significant anisotropy in mechanical behavior and failure strength can arise from planar rock fabrics such as bedding in sedimentary rocks, cleavage in slates, as well as preferred orientation or arrangement of minerals and cracks in igneous and metamorphic rocks. The anisotropy of tensile and compressive strengths may be associated with different failure modes and deformation mechanisms, depending on how stress is applied relative to the anisotropy planes (Baud *et al.*, 2005).

Extensive studies have been conducted on the brittle strength of anisotropic rocks as a function of the angle θ between the maximum principal stress and the foliation or bedding. In relatively compact rocks (such as slate, phyllite, schist, gneiss and amphibolite) as well as in more porous rocks such as shale, the brittle strength

---

[1] Département des Sciences de la Terre et de l'Environnement, Université de Cergy-Pontoise, CNRS UMR 7072, Bâtiment Neuville 3.1, Neuville-sur-Oise, F-95031 Cergy-Pontoise, France.
E-mail: laurent.louis@u-cergy.fr
[2] Institut de Physique du Globe (CNRS/ULP), 5 rue Descartes, 67084 Strasbourg, France.
[3] Department of Geosciences, State University of New York, Stony Brook, NY 11794-2100, USA.

anisotropy is characterized by a minimum in the peak stress at $\theta = 30–45°$ and maxima at $\theta = 0°$ and $90°$. Such strength anisotropy can be interpreted by a model with the foliation or clay-rich bedding acting as "planes of weakness" that promotes frictional slip and wing crack growth (e.g., WALSH and BRACE,1964; RAWLING *et al.*, 2002; JAEGER and COOK, 1979). However, the anisotropic behavior is fundamentally different in a porous sandstone, the strength of which may attain maximum and minimum values at $\theta = 90°$ (perpendicular to bedding) and $\theta = 0°$ (parallel to bedding), respectively. As reviewed by BAUD *et al.* (2005), many questions related to the mechanics of anisotropic failure in porous sandstone remain unanswered.

What are the actual microstructural attributes that govern the apparent influence of bedding on failure in an anisotropic porous sandstone? In response to an applied deviatoric stress field, the pore space in the rock may dilate or compact, and the brittle-ductile transition is sensitively dependent on the interplay of dilatancy and compaction. How does bedding influence the onset and development of compactive yield, and to what extent can bedding anisotropy influence the development of strain localization and failure modes associated with the brittle-ductile transition? We chose the Rothbach sandstone, the anisotropic behavior of which had been investigated focusing on the two end-members represented by samples cored perpendicular and parallel to bedding (WONG *et al.*, 1997; BAUD *et al.*, 2005; LOUIS *et al.*, 2007a). In this study, a series of new experiments were performed on "oblique" samples cored at $45°$ with respect to the bedding. Systematic microstructural investigation on undeformed and deformed samples were conducted using optical and electron microscopy, as well as X-ray CT-imaging.

2. Characterization of Microstructural Inhomogeneity Associated with Bedding

The Rothbach sandstone belongs to the Lower Triassic "Vosgian sandstone" formation, with extensive outcrops on either side of the Rhine Graben in northeastern France and southwestern Germany. Reddish in color, the Rothbach sandstone formed from cross-bedded, fluvial sediments and has been widely used as a building stone. It has been the focus of various studies on mechanical (DAVID *et al.*, 1994; WONG *et al.*, 1997; BÉSUELLE *et al.*, 2003; BAUD *et al.*, 2004) and other physical (ZHU and WONG, 1997; LOUIS *et al.*, 2005) properties.

Our samples were cored from the block studied by BAUD *et al.* (2004), with initial porosity of $20 \pm 1\%$. Its modal composition is 68% quartz, 16% feldspar, $\sim 12\%$ clays, 3% oxides and mica (DAVID *et al.*, 1994). Optical microscope observations of LOUIS *et al.* (2005) indicate a granulometric layering, that alternates between zones with significant contrasts in porosity and grain size. Whereas the more porous layers have coarser grains (with diameters in the range 200–250 μm), the more compact layers have finer grains (with diameters in the range 100–150 μm). The more compact layers (with thicknesses down to 1 mm) are significantly thinner than the more porous zones (with thicknesses up to 1 cm). LOUIS *et al.* (2005) observed that a majority of grains in Rothbach sandstone were

preferentially elongated along the bedding plane, and that the intergranular contacts were as well aligned preferentially with bedding. They suggested that these microstructural attributes may collectively contribute to elastic anisotropy (on the order of 5%), as manifested by a relatively high P-wave velocity measured perpendicular to the bedding. An objective of this study is to characterize quantitatively such microstructural inhomogeneities.

2.1. X-ray-computed Tomography: Density and Porosity Contrasts

To characterize quantitatively the density and porosity contrasts associated with bedding and its spatial distribution, we used the High-Resolution CT Facility at the University of Texas at Austin to scan the Rothbach sandstone samples. The facility there employed a 200 kV microfocal X-ray source capable of a < 10 μm focal spot size, and our data were typically acquired with the source at a peak energy of 180 kV. The methodology for data acquisition and analysis was described in KETCHAM and ITURRINO (2005) and KETCHAM and CARLSON (2001).

We show in Figure 1a an image (with voxel dimension 50 μm) for an undeformed sample cored oblique to the bedding plane. The grey level of a voxel in the image corresponds to the CT-number, which is related to the attenuation of X-ray passing through the porous material. While the attenuation in a solid mineral is predominantly controlled by the atomic number of its elements, its value in a porous material is also dependent on the density, and hence sensitive to the local porosity in a voxel (KETCHAM and CARLSON, 2001). In Figure 1a, the sedimentary layering is manifested by relatively light narrow zones corresponding to dense laminations. In this sandstone sample, we visually isolated 11 zones of alternating high and low porosity.

If the spatial distribution of minerals in the solid matrix is relatively homogeneous, then the average CT-number in a given area can be approximated as linearly related to the porosity (VINEGAR et al., 1991; DESRUES et al., 1996). In a plot of the grey level versus density (Fig. 1b), this linear relation can be established by connecting a straight line between the two points corresponding to the grey level of the void space (with zero density) and the mean grey level of the sample image (with an average density of 2070 kg/m^3 for our sandstone). Using this linear relation, the density of a subset of the sample can then be inferred from the mean grey level of the voxels embedded in this subset. As illustrated in Figure 1c, the 11 zones identified in Figure 1a have distinct mean values of grey level, implying distinct values of average local density (Fig. 1c). The inferred density variation among the 11 zones in the sample is about ± 5% with reference to the bulk density of 2070 kg/m^3 for the entire sample. If we assume a porosity value of 20.4% (which corresponds to the arithmetic mean for > 30 samples cored in the same block), we can infer the local porosity of the 11 zones from these density estimates (Fig. 1a). We thus infer that the presence of bedding in this sample of Rothbach sandstone is associated with significant contrasts in porosity, ranging from 15.8% to 23.7%.
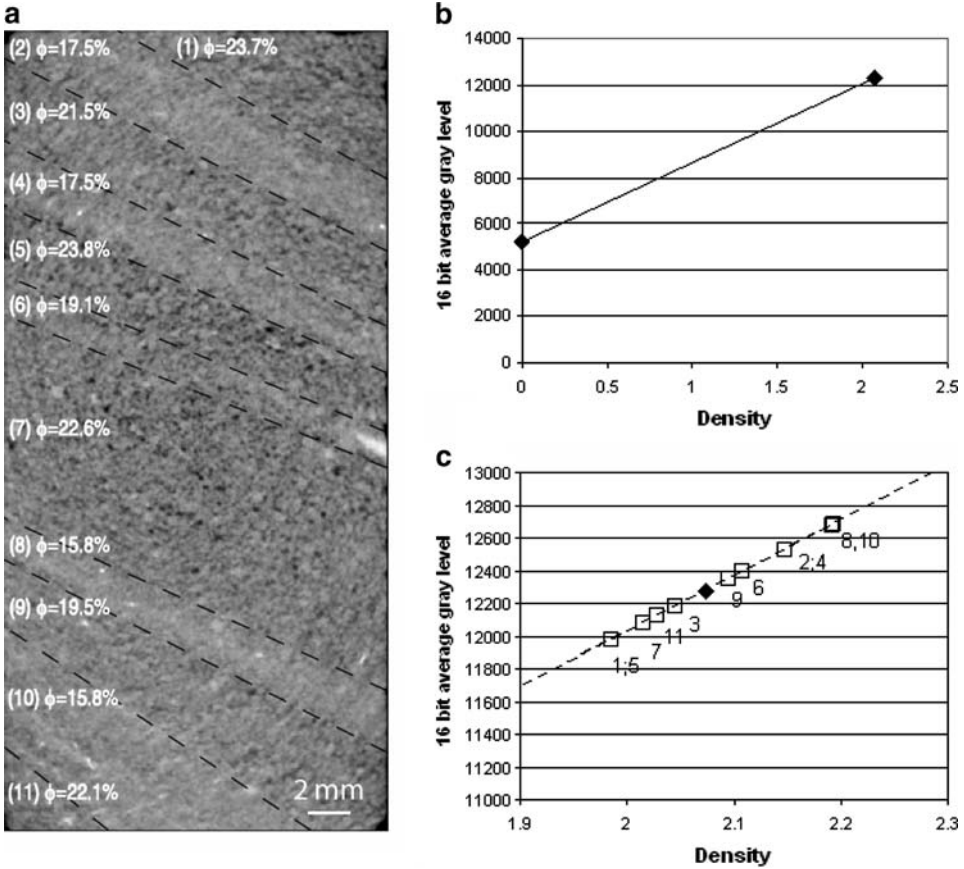
Figure 1

a. X-ray CT scan of a sample of Rothbach sandstone cored at ∼ 45 degrees to the bedding and porosity values in visually identified regions derived directly from density in Figure 1c assuming a porosity of 20.4% for the entire sample image. b. *Ad hoc* calibration line retrieved from the CT scan image. c. Position of the zones isolated in a. on the calibration line assuming a linear relationship between average grey level and effective density.

2.2. Scanning Electron Microscopy: Anisotropy of Intergranular Contact Normal

A backscattered scanning electron microscope (SEM) image of the grain and pore structure is presented in Figure 2a. The bedding of this sample was sub-horizontal. It can be observed that the quartz grains and lithic fragments of quartz and K-feldspar are well cemented and coated by clay minerals (mostly illite as determined by semi-quantitative X-ray-based elemental mapping under the SEM). Similar features were observed under the laser scanning confocal microscope (LOUIS *et al.*, 2005). Details of an intergranular contact in one of the more porous (and relatively thick) zones as revealed by backscattered SEM (Fig. 2b) is contrasted with an image of the same area observed by cathodoluminescence (CL) SEM (Fig. 2c). Since CL-SEM can distinguish different
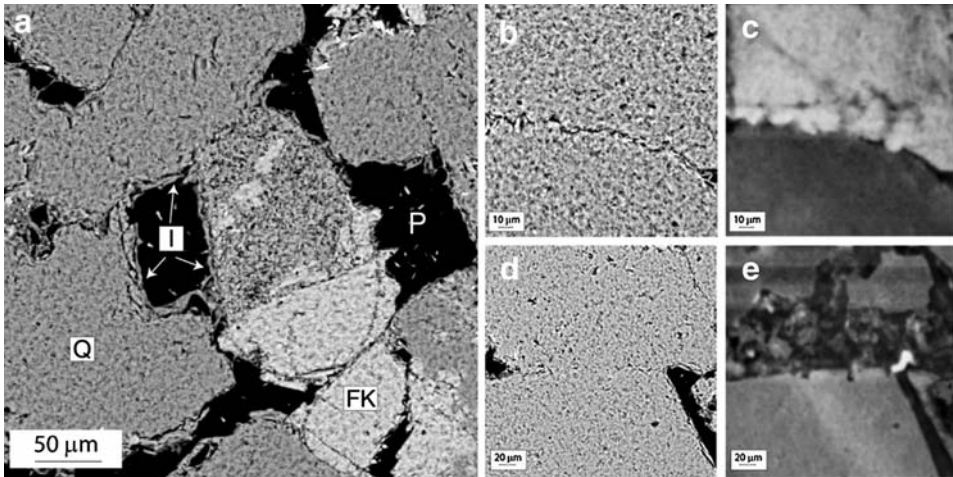
Figure 2

a. Scanning electron microscope image (BSE – backscattered electrons) of the Rothbach sandstone. Grains and lithic clasts of quartz (Q) and K-feldspar (FK) are coated with clays (mostly illite, denoted by Il). The pore space is denoted by P. b. BSE image of a grain contact in relatively high porosity zone. c. Cathodoluminescence image of the grain contact in b. d. BSE image of a grain contact in relatively low porosity zone. e. Cathodoluminescence image of the grain contact in d.

diagenetic generations of crystallization, healed cracks and crushed grains that were subsequently lithified which were not resolved by backscattered SEM are imaged in Figure 2c. Similarly, Figures 2d and 2e present backscattered and CL images, respectively, of an intergranular contact in one of the more compact (and relatively thin) zones. For either intergranular contact, the geometry of the contact and damage zone suggest that relatively intense compaction occurred after deposition and that the effective contacting surface was enhanced sub-parallel to bedding.

To characterize the contact length distribution and its anisotropy, ~ 1700 intergranular contacts located in both low and high porosity areas were randomly selected from a mozaic of SEM images of a sample with sub-horizontal bedding. Bedding is described here as sub-horizontal due to its crosscut nature and fuzzy boundaries between layers. The total surface investigated was about $6*20$ mm^2. Each grain contact was approximated by a linear segment, the length and orientation of which were measured. Figure 3a shows the angular variation (in bins of 5°) of the contact normals so measured. The most populated angular classes of contact normal are located close to the top direction of the image that was used for the analysis. In Figure 3a we also plot the contact length as a function of its orientation (represented by an angle that is complementary to the normal direction). Compared with the contact normal distribution, even though the anisotropy of contact length is not as pronounced, it still shows an overall trend for longer contacts to be close to horizontal.
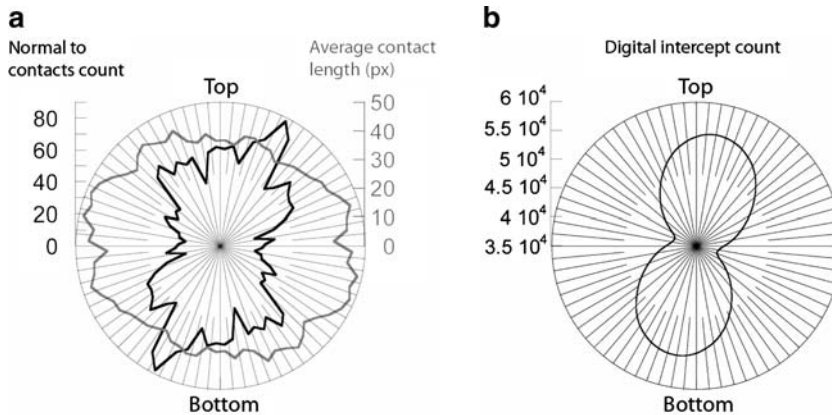
Figure 3

a. Preferred intergranular contact orientation and average length as a function of the observation angle from a SEM mosaic with nominally horizontal bedding. b. Digital intercept density taking into account both length and orientation of the intergranular contacts. Larger effective contacting surface dips 10–15 degrees to the right.

We also conducted measurement of the angular distribution of linear intercept density for this population of ~ 1700 grain contacts. The linear intercept density is a stereological parameter defined as the number of intersections between a test array of parallel lines and a population of objects, normalized by the total length of the test array (UNDERWOOD, 1970). The anisotropy can be characterized by using arrays in different orientations. On our digital image showing all the grain contacts, an automated procedure was developed to count the number of intercepts made by the intergranular contacts with 180 test arrays at angles varying from $0°$ to $179°$. Such stereological measurements map out the anisotropic distribution of contact length per unit area as imaged on the two-dimensional section. If the distribution in the cylindrical sample can be approximated as axisymmetric, then the stereological data can also be related to the anisotropic distribution of contact area per unit volume in the sandstone. Our data in Figure 3b indicate a maximum intercept density at $11°$ to the vertical, which corresponds to a maximum specific surface area for intergranular contacts oriented at $11°$ to horizontal. Since the bedding in this sample is sub-horizontal, this implies an overall trend for the intergranular contacts to align in orientations sub-parallel to bedding.

3. Mechanical Deformation and Failure Mode

To complement the data sets of WONG *et al.* (1997) and BAUD *et al.* (2005) for Rothbach sandstone samples cored parallel and perpendicular to bedding, in this study we focused our mechanical tests on samples cored at an oblique angle of $\sim 45°$ to bedding. In addition, selected tests were conducted on samples cored parallel and perpendicular to

the bedding to acquire a more complete data set for all three orientations at several effective pressures (Table 1). The samples were cylinders with diameter of 18.4 mm and length of 38.1 mm. They were saturated with deionized water and deformed between lubricated end caps in conventional triaxial tests under drained conditions at a constant pore pressure of 10 MPa. The tests were performed at room temperature, axial strain rate of $1.3 \times 10^{-5} \, s^{-1}$ and effective pressures ranging from 5 to 250 MPa. The volume change was approximated by the ratio of the pore volume change (given by the pore volumometer DCDT) to the initial bulk volume of the sample (WONG et al., 1997). The acoustic emission (AE) activity was pre-amplified and discriminated from electric noise using signal amplitude and frequency characteristics (ZHANG et al., 1990).

In the following, we will use the convention that compressive stresses and compactive strains are positive. Maximum and minimum compressive stresses will be denoted by σ_1 and σ_3, respectively. We will denote the pore pressure by P_p, the confining pressure by P_c ($P_c = \sigma_2 = \sigma_3$) and the difference between the confining pressure and the pore pressure ($P_c - P_p$) by P_{eff} (effective pressure). The effective mean stress $(\sigma_1 + 2\sigma_3)/3 - P_p$ will be denoted by P and the differential stress $(\sigma_1 - \sigma_3)$ by Q.

We will refer to samples that were cored perpendicular, parallel and at $\sim 45°$ degrees to bedding as "perpendicular", "parallel" and "oblique", respectively.

3.1. Stress-strain Data and Acoustic Emission Activity

Figure 4 presents the data of a hydrostatic compaction test for an oblique sample, showing the effective pressure as a function of the porosity reduction. In such a hydrostat for a porous rock, one typically observes an inflection point P^* that corresponds to the critical effective pressure for the onset of grain crushing and pore collapse. In a porous sandstone, this grain crushing pressure is primarily controlled by the porosity and grain size (ZHANG et al., 1990). For this particular experiment, we obtained a value of 239 MPa for P^*. A total of eight tests performed on perpendicular, oblique and parallel samples gave an average value of 237 MPa for P^* (see also Table 1).

We also present in Figure 4 the results of two conventional triaxial tests on oblique samples deformed at 5 MPa and 150 MPa effective pressure. If the porosity change was solely controlled by the effective mean stress, then the triaxial curves should coincide with the hydrostat, and any deviation would indicate that the differential stress also contributes to porosity change. In the test at 150 MPa effective pressure, we observed an accelerated porosity reduction that initiated at the critical stress state indicated by C^*, which thus marked the onset of "shear-enhanced compaction" (WONG et al., 1997). In contrast, in the test at 5 MPa, the porosity reduction was observed to decelerate with respect to the hydrostat at the critical stress state indicated by C', which thus marked the onset of dilatancy.

In Figures 5a-b and Figures 5c-d we compare the mechanical data for perpendicular, oblique and parallel samples deformed at these two effective pressures. At relatively low confinement (5 MPa effective pressure), the mechanical responses for

Table 1

Compilation of all mechanical data for the three coring directions investigated

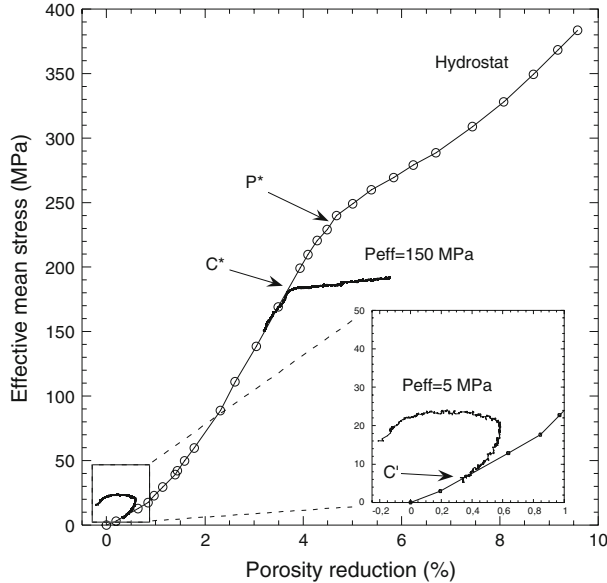|	Effective stress σ_3–P_p (MPa)	Regime (B):brittle (C):compactive + (d):dilatancy	Mean and differential stresses at failure ( ) Onset of shear-induced dilation C′	
			$(\sigma_{1+2}\sigma_3)/3$-P_p (MPa)	σ_1−σ_3 (MPa)
Perpendicular	5	(B) + (d)	26 (13)	61 (24)
	10	(B) + (d)	35 (15)	74 (15)
	20	(B) + (d)	52 (38)	95 (54)
	35	(B) + (d)	77.5 (55)	127 (60)
	40	(B)	77.5	111
	55	(C)	97	124
	55	(C)	99	130
	90	(C)	131	122
	110	(C)	161	137
	130	(C)	172.5	123
	130	(C)	173	125
	150	(C)	193	126
	165	(C)	202	112
	240	(C)	240	0
	245	(C)	245	0
	245	(C)	245	0
Oblique (∼45 deg)	5	(B) + (d)	24 (8)	54 (9)
	10	(B) + (d)	31 (15)	62 (15)
	20	(B)	50	86
	30	(B)	65	103
	55	(C)	95	116
	90	(C)	127	108
	130	(C)	163	98
	150	(C)	182	93
	170	(C)	199	82
	190	(C)	214	70
	238	(C)	238	0
	239	(C)	239	0
Parallel	5	(B) + (d)	22 (16)	48 (33)
	10	(B) + (d)	30 (21)	58 (33)
	20	(B) + (d)	47 (28)	80 (24)
	30	(B)	57	82
	50	(C)	80	90
	55	(C)	88	97
	90	(C)	124	99
	115	(C)	150	102
	130	(C)	161	91
	130	(C)	162	94
	140	(C)	168	84
	150	(C)	177.5	79
	190	(C)	204	38
	200	(C)	210	30
	220	(C)	220	0
	234	(C)	234	0
	238	(C)	238	0

Figure 4

Hydrostatic compaction test ($\sigma_1 = \sigma_2 = \sigma_3$) for a sample of Rothbach sandstone and results of two triaxial experiments in an effective mean stress vs. porosity reduction plot. The effective stress corresponding to the onset of grain crushing and pore collapse in the hydrostatic tests (~ 239 MPa) is denoted by P^*. For the triaxial test at $P_{eff} = 5$ MPa, porosity change decelerates with respect to the hydrostat at a critical stress state marked by C' (shear-induced dilation). For the triaxial test at $P_{eff} = 150$ MPa, an accelerated porosity decrease occurs at the critical stress state C^* (shear-enhanced compaction).

all three orientations are typical of the brittle faulting regime. The differential stress as a function of axial strain attains a peak, and then the sample strain softens while the differential stress drops to a residual level (Fig. 5a). With reference to the hydrostat, the data for effective mean stress as a function of porosity reduction (Fig. 5b) indicate the onset of dilatancy in the pre-failure stage before reaching the peak stress. Our data indicate that the maximum, intermediate and minimum values of peak stress were associated with the perpendicular, oblique and parallel samples, respectively.

At relatively high confinement (150 MPa effective pressure), the mechanical responses for all three orientations are typical of the cataclastic flow regime. The differential stress continues to increase as a function of axial strain, characteristic of strain hardening behavior (Fig. 5c). With reference to the hydrostat, the data of effective mean stress as a function of porosity reduction (Fig. 5d) indicate the development of shear-enhanced compaction in all three orientations. Our data indicate that the maximum, intermediate and minimum values of the critical stress for the onset of shear-enhanced compaction were associated with the perpendicular, oblique and parallel samples, respectively.
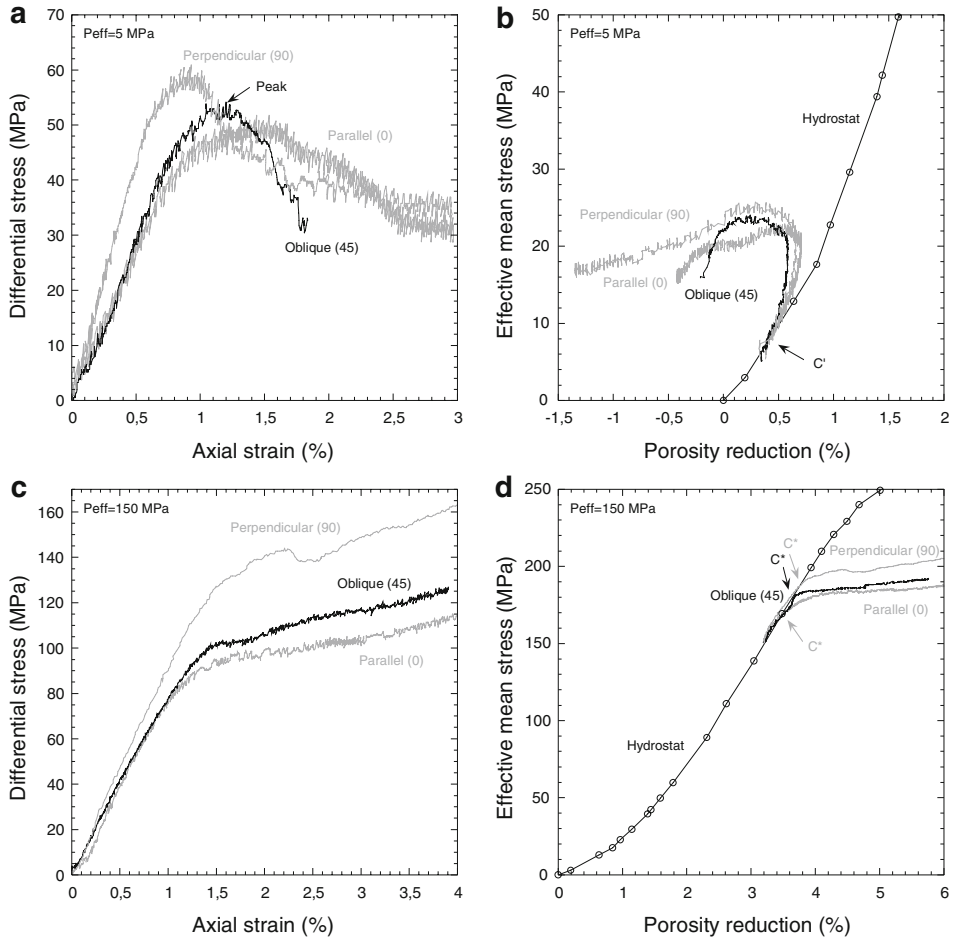
Figure 5

Example of mechanical data obtained for perpendicular, oblique and parallel samples at low (5 MPa) and high (150 MPa) effective pressure. a. Stress vs. strain curve at 5 MPa effective pressure. b. P vs. porosity reduction at $P_{eff} = 5$ MPa. c. Stress vs. strain curve at $P_{eff} = 150$ MPa. d. P vs. porosity reduction at $P_{eff} = 5$ MPa. For both values of P_{eff}, oblique samples have intermediate mechanical strength between perpendicular and parallel samples.

We compile in Figure 6 the stress-strain curves for all 6 oblique samples deformed at effective pressures ranging from 55 MPa to 190 MPa. The AE activities recorded in these experiments (except for the one at 55 MPa) are also presented. The data for 130 MPa effective pressure were previously presented by LOUIS *et al.* (2007a), who compared the AE activity of this oblique sample with a perpendicular and a parallel sample deformed at the same effective pressure. They noted subtle differences in AE activity among these three samples when stressed to beyond the onset of shear-enhanced compaction. Whereas
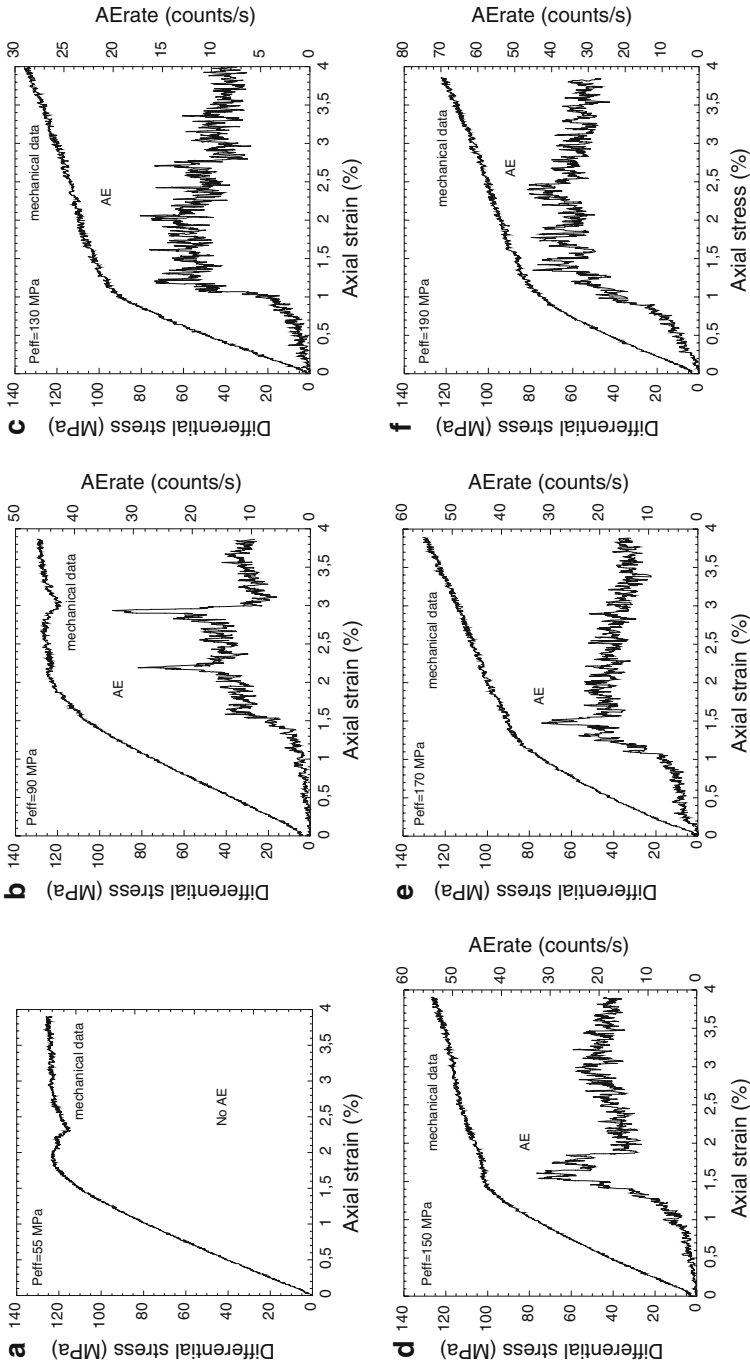
Figure 6

a.-f. Differential stress Q and acoustic emission rate vs. axial strain at $P_{eff} = 55$ MPa, 90 MPa, 130 MPa, 150 MPa, 170 MPa and 190 MPa for oblique samples.

distinct upsurges in AE activity were observed in both the oblique and perpendicular samples, AE rate in the parallel sample seemed almost constant. In light of the conclusion of BAUD *et al.* (2004) that such differences in AE activity may signify differences in failure mode, the data therefore suggest the possibility that these samples cored in different orientations may have failed by different modes of strain localization. The data in Figure 6 show that the AE activities in oblique samples deformed at effective pressures of 90, 150, 170 and 190 MPa were qualitatively similar to the 130 MPa sample, in that the development of shear-enhanced compaction was manifested by at least one AE upsurge, which was sometimes accompanied by a small stress drop on the order of 10 MPa.

3.2. Brittle Strength and Compactive Yield Stress

In Figure 7a, we compiled in the *P-Q* space data on brittle strength and the stress state at the onset of shear-enhanced compaction C* of Rothbach sandstone for the three coring directions investigated (cf., Table 1). We plot the peak stress for samples that failed by brittle faulting and the differential stress at the onset of shear-enhanced compaction. We also plot in Figure 7b these critical stresses as functions of angle θ between the maximum principal stress and the bedding. There appears to be an overall trend for the maximum, intermediate and minimum values of both the brittle strength and compactive yield stress (at the same effective mean stress) to be associated with the perpendicular, oblique and parallel samples, respectively. This result contrasts chiefly with the frequent observation that strength is minimum at 30–45 degrees with respect to the bedding plane in a layered material.
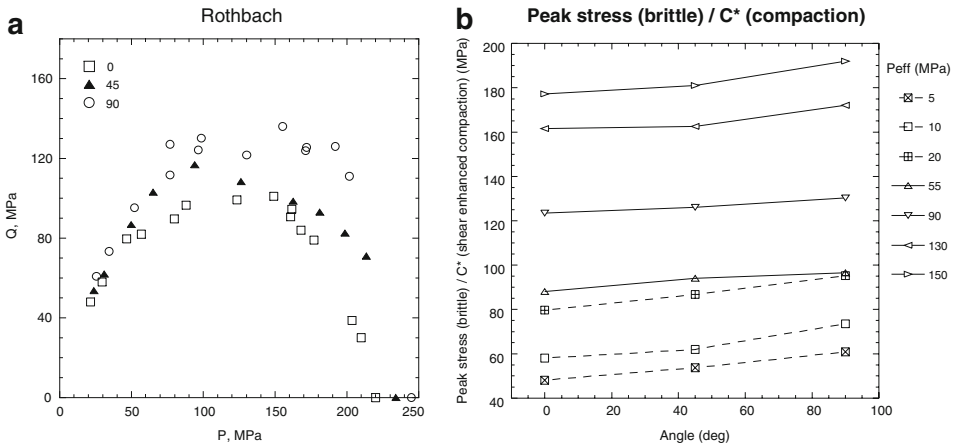

Figure 7

a. *Q* vs. *P* plot at the peak of the stress/strain curve (brittle regime) and at *C** (compactant regime) for all samples studied. Oblique samples yield at intermediate values of *Q*. b. Peak stress (square symbols) and *Q* at C* (triangles) as a function of the sample orientation for all triplets available.

Our brittle strength data for Rothbach sandstone are in basic agreement with the more systematic investigation on Adamswiller sandstone by MILLIEN (1992), who deformed nominally dry samples cored in seven bedding orientations (0°, 15°, 30°, 45°, 60°, 75° and 90°) at six fixed confining pressures ranging from room pressure to 50 MPa. They observed a general trend for the brittle strength to gradually decrease with decreasing angle, from a maximum for the perpendicular sample (90°) to a minimum for the parallel sample (0°). The brittle failure envelope for our oblique samples seems to fall very close to that of the perpendicular samples. However, it should be noted that duplicate experiments indicate significant sample-to-sample variability in the brittle strength. In contrast, the data for the compactive yield stresses were not as variable. Although previous studies (e.g., WONG *et al.*, 1997) have investigated the yield stress contrast between samples cored perpendicular and parallel to bedding, to our knowledge this is the first systematic measurement of the yield stress of porous sandstone samples cored in an oblique direction. Our data demonstrate that in general, the compactive yield stress of an oblique sample is intermediate between those of the parallel and perpendicular samples. It is likely that the compactive yield stress follows a trend similar to that for the brittle strength, showing a progressive decrease with decreasing angle, from a maximum for the perpendicular sample (90°) to a minimum for the parallel sample (0°).

3.3. Failure Mode and Spatial Distribution of Damage

Thin sections of the failed samples were prepared along a surface parallel to the sample axes. For the parallel and oblique samples, sections were prepared so that the strike of the bedding would be perpendicular to the observation plane. The oblique sample that failed at 10 MPa effective pressure was sent to the High-Resolution CT Facility at the University of Texas at Austin for a full scan at 50 μm resolution, then a thin section cut parallel to the sample axis was prepared for observation under the microscope. To characterize the spatial distribution of damage, we adopted the technique of MENÉNDEZ *et al.* (1996). The thin section of a failed sample was divided into elemental squares and each square was then assigned a damage index on the basis of optical microscope observations. If n denotes the average number of cracks per grain, then index values of I, II, III and IV correspond to $n < 2$, $2 \leq n < 5$, $5 \leq n < 10$, and $n > 10$, respectively. The damage was determined for two oblique samples compacted at effective pressures of 130 MPa and 190 MPa, using elemental squares with widths of 0.75 mm and 1.00 mm, respectively.

3.3.1 Brittle failure. At effective pressures of 5 MPa, 10 MPa and 30 MPa, shear bands were observed to develop in the failed samples for all three orientations we investigated. Our microstructural observations focused on the oblique samples.

Figure 8a shows a X-ray scan of the oblique sample that failed at 10 MPa effective pressure. The scan corresponds to an axial plane that cut through the sample. Slight bulging of the bottom part of the sample was observed, together with an open shear band
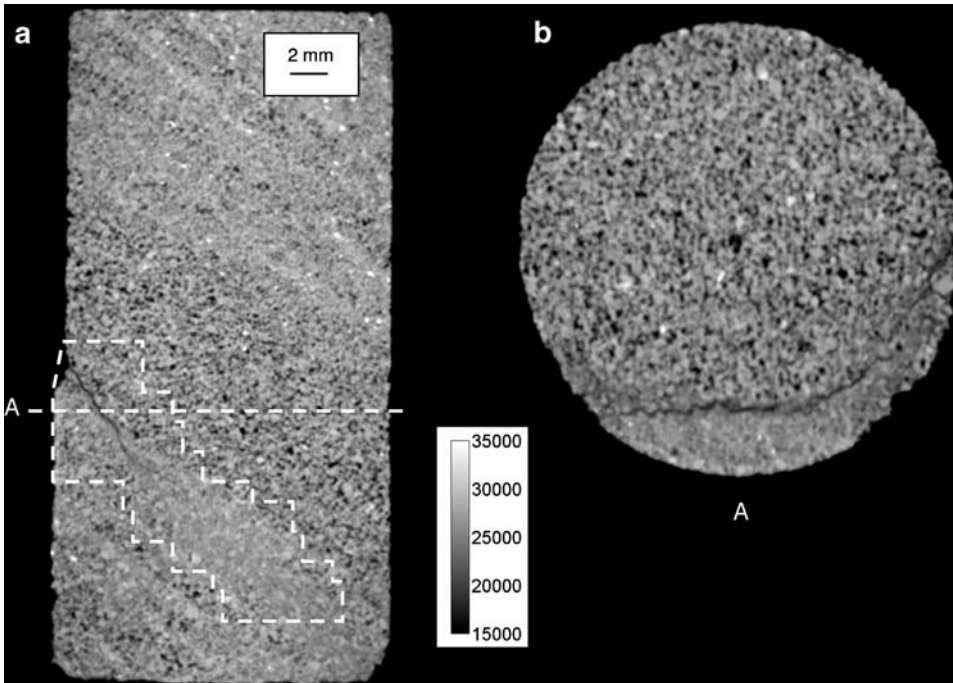
Figure 8
X-ray scan of an oblique sample deformed at $P_{eff} = 10$ MPa. a. Vertical section containing the sample axis.
b. Basal plane section at height ~ 16 mm.

emanating from the sample surface. The grey level contrast between nominally undeformed parts on either side of the open fracture suggests that the shear band propagated close to an interface between two zones of contrasting porosities and/or average grain sizes. In Figure 8b we present a transverse cross section (cut parallel to the basal plane of the sample) at the height of ~ 16 mm, as marked by the dotted line in Figure 8a. The shear band maps out a somewhat tortuous arc that extended across the section, and again the contrast in grey level suggests a propagation in the vicinity of a strong porosity gradient (porosity estimations using the method presented in section 2.1. provided values of respectively 19.7% and 25.0% for the lower and higher porosity zones).

A mosaic (overlapping with the region enclosed by the dotted contour in Figure 8a) was acquired under the optical microscope in reflected light (Figs. 9a-c). Damage in the form of intensely cracked grains was observed in the shear band, which cut through the section along a somewhat tortuous path with apparent thickening near the bottom of the sample. The angle of the shear band with respect to the vertical axis of the sample is $\sim 40°$, which is appreciably higher than the $\sim 30°$ angle for perpendicular Rothbach sandstone samples that was reported by BÉSUELLE *et al*. (2000). It should also be noted
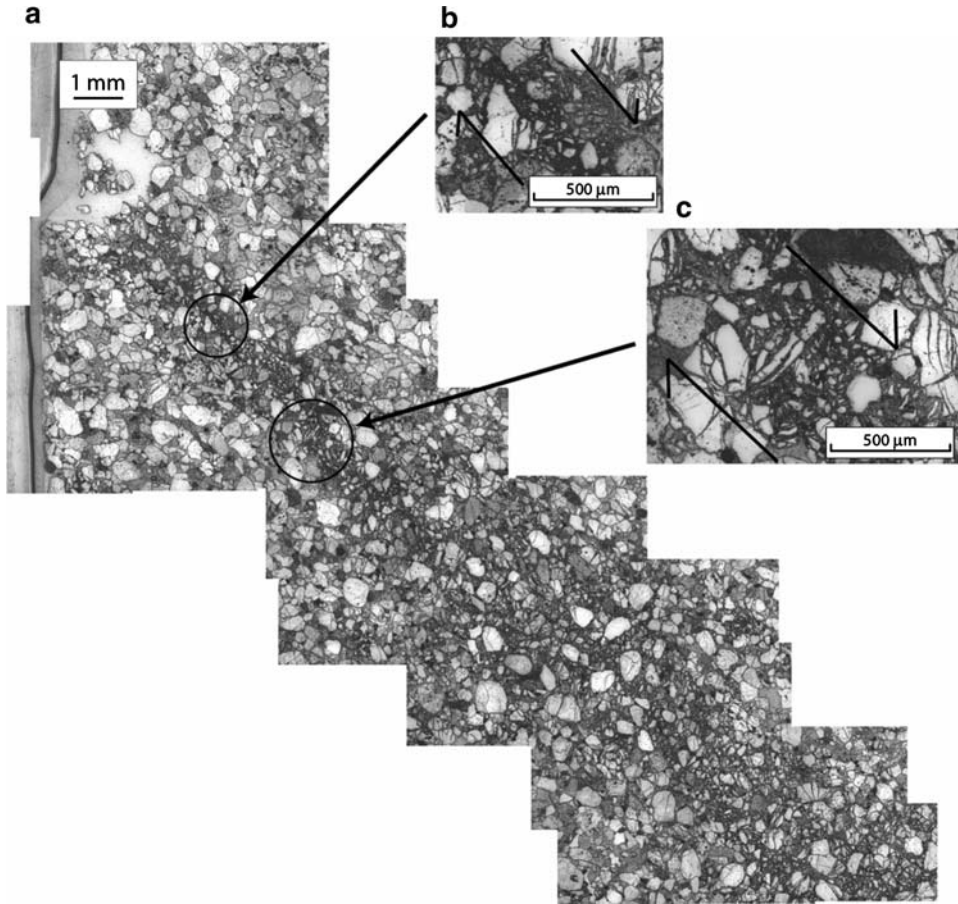
Figure 9
a. Optical microscope image mosaic corresponding to the area traced in Figure 8a. b,c. Intense damage and indications of shear are found across the localized band.

that in comparison to their perpendicular samples, the shear band analyzed here is not as geometrically complex. This difference is in basic agreement with MILLIEN's (1992) observations on Adamsviller sandstone. She concluded that when samples were cored along a direction oblique to the bedding plane, the strike of the shear band would almost systematically lie parallel to bedding.

3.3.2 Shear-enhanced compaction. Previous investigations of the damage evolution related to compactive yield are restricted to perpendicular and parallel samples. In a perpendicular sample of Rothbach sandstone failed at 130 MPa effective pressure, the microstructural observations and stereological data of BÉSUELLE *et al.* (2003) demonstrate the development of several diffuse compaction bands with intense damage that are subparallel to bedding. BAUD *et al.* (2004) suggested that the development of each of

these diffuse compaction bands was probably manifested by a distinct upsurge in AE activity, and that the localized damage first initiated near an interface and then propagated laterally to form a relatively diffuse band within the more porous zone between neighboring bedding planes.

In contrast, the damage in a parallel sample was observed to be more diffuse, and as noted earlier, the AE activity did not show any discrete surge. In a parallel sample of Rothbach sandstone failed at 130 MPa effective pressure, BAUD *et al.* (2005) documented relatively short segments of elongate damage subperpendicular to σ_1. The overall damage was distributed homogeneously in that although elongate clusters had developed, they did not propagate all the way across the sample, possibly because the bedding planes inhibited their continuous growth.

Such fundamental differences in the spatial pattern of damage between a perpendicular and a parallel sample were further documented by LOUIS *et al.* (2007a). In particular, they studied an oblique sample failed at effective pressure of 130 MPa, and here we extended this previous study to also analyze an oblique sample failed at 190 MPa. In Figures 10a-c, we present the spatial distributions of damage in the perpendicular, oblique and parallel samples failed at 130 MPa. In contrast to the delocalized pattern of damage in the parallel sample, a number of diffuse, elongate zones of intense damage subparallel to bedding can be identified in both the perpendicular and oblique samples. As noted earlier, distinct upsurge in AE activity were observed in both perpendicular and oblique samples, which may be related to the propagation of these diffuse bands. Taking into account their kinematics relative to the σ_1 orientation, these diffuse bands can be categorized as compaction bands and compacting shear bands, respectively.

Our data for the oblique sample failed at 190 MPa effective pressure (Fig. 11a) show a damage pattern qualitatively similar to the compacting shear band in the 130 MPa sample. We also performed a more refined damage mapping of this sample. Under relatively high magnification, small elemental areas (~ 50 μm wide) were analyzed and those associated with intense grain crushing (with damage index = IV) were pinpointed on the image. In Figure 11b the dark areas correspond to these intensely damaged clusters, which are heterogeneously distributed within what appears as diffuse bands in Figure 11a under lower magnification. This observation at higher resolution reveals the presence of short subhorizontal elongated patches, what suggests possible band propagation on short distances in higher porosity zones.

4. Discussion

4.1. Microstructural Origin of the Mechanical Anisotropy

For several decades, numerous studies have been conducted on the brittle strength of anisotropic rocks as a function of the angle θ between σ_1 and the foliation or bedding.
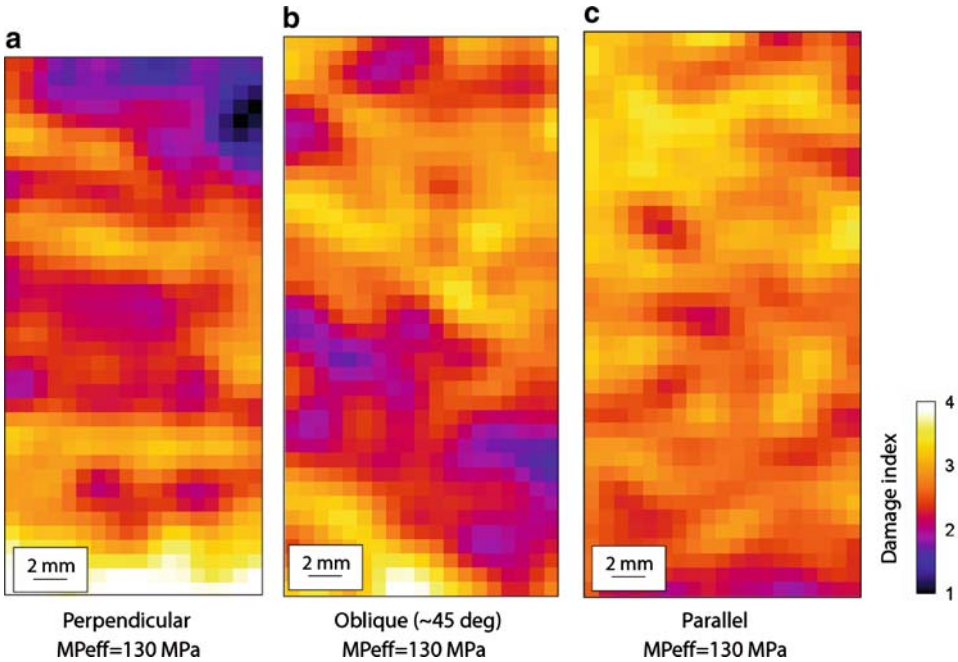
Figure 10

a.-c. Damage maps obtained by Louis *et al.* (2007a) on thin sections of samples deformed at $P_{eff} = 130$ MPa. Each cell is attributed a damage index value between 1 and 4 based on the average number of cracks per grain (cf., section 3.3).

Baud *et al.* (2005) noted that two types of anisotropic behavior should be distinguished. The first type of brittle strength anisotropy manifested by a minimum in the peak stress at $\theta = 30$–$45°$ and maxima at $\theta = 0°$ and $90°$, has been widely observed in relatively compact rocks such as slate, phyllite, schist, gneiss and amphibolite, as well as in more porous rocks such as shale. Such strength anisotropy can be interpreted by a model with the foliation or clay-rich bedding acting as "planes of weakness" that promotes frictional slip and wing crack growth (e.g., Walsh and Brace, 1964, Rawling *et al.*, 2002).

The second type of behavior commonly observed in porous sandstones is manifested by a progressive decrease of brittle strength with bedding angle, with a maximum at $\theta = 90°$ (perpendicular to bedding) and minimum at $\theta = 0°$ (parallel to bedding). Rothbach sandstone has this type of strength anisotropy, and our microstructural observations have provided some insights into the micromechanics. According to our CT data (Fig. 1), the thin bedding planes are relatively compact and fine-grained. Therefore one would expect them to be stronger than the more porous and thicker zones outside. Hence the bedding in a porous sandstone may actually represent planes of relative strength (and not weakness), and accordingly the strength anisotropy in a porous sandstone is fundamentally different from that in a foliated metamorphic rock or shale.
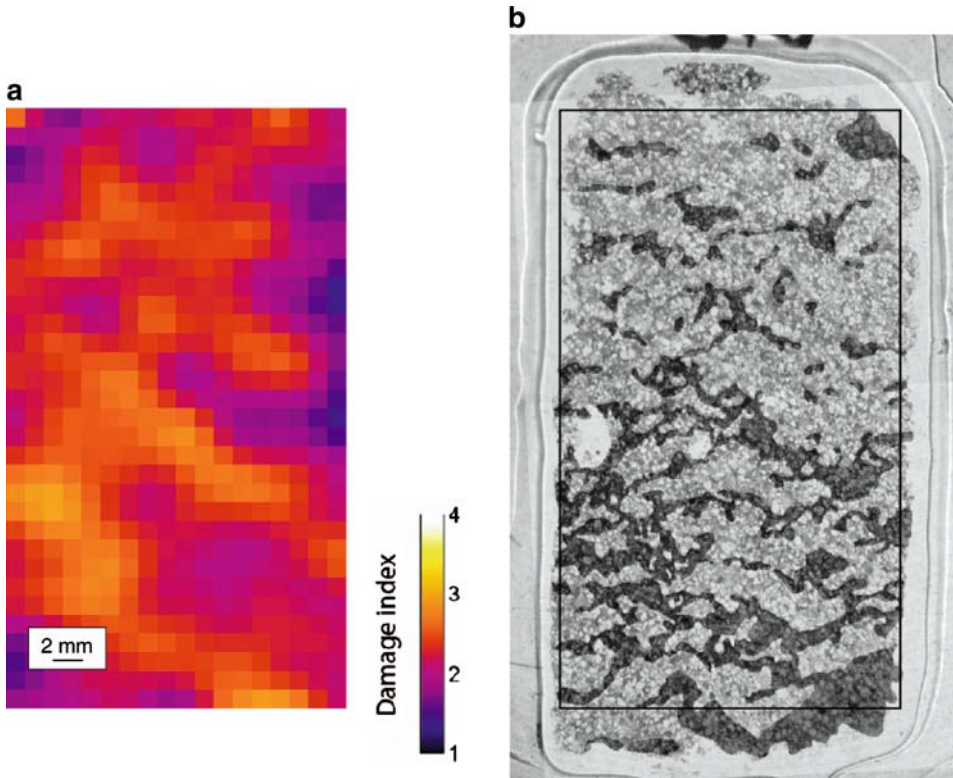
Figure 11
a. Damage map obtained from a thin section of the oblique sample deformed at $P_{eff} = 190$ MPa. b. High resolution damage mapping based on direct microscope observation for the sample deformed at $P_{eff} = 190$ MPa. Damage zones are represented with their actual extent. Deformation appears more localized than in Figure 11a with highly tortuous compaction structures.

Given the porosity (and inferred strength) contrast, a plausible model for the strength anisotropy is that of a composite with strong layers bonded to a relatively weak matrix. This class of model has been widely analyzed in the mechanics of composite materials (e.g., HULL, 1981), and it typically predicts the composite to have maximum and minimum strengths at $\theta = 0°$ and $\theta = 90°$, respectively. This model prediction is diametrically opposite to laboratory observations on porous sandstones (Fig. 7).

There are at least two microstructural attributes that are not being considered in this idealized model. First, in fluviatile sandstone such as the one studied here, the boundaries between relatively compact and more porous zones are likely to be rather diffuse and irregular. Moreover, mechanical heterogeneities inherent to granular assemblies are believed to play an important role in damage nucleation and propagation. In the case of parallel samples, which are the ones that would be expected to be mechanically stronger according to the conceptual layered model, failure may in fact occur through the

solicitation of mechanically weaker zones outside the denser layers. Second, the development of grain-scale damage in a porous sandstone is strongly influenced by geometry and cementation of the intergranular contacts (e.g., MENÉNDEZ et al., 1996; WONG and WU, 1995). Our new data on the anisotropic distributions of grain contact number and length (Fig. 3) suggests that these features could be for a significant part responsible for the observed mechanical anisotropy. This potential influence on brittle strength anisotropy should probably be incorporated into a more realistic micromechanics model.

In this study we have demonstrated that the anisotropies of compactive yield stress and brittle strength are qualitatively similar, and it is therefore likely that the two microstructural attributes discussed above can exert analogous control over both modes of failure. Our data also underscore the important influence of bedding on mode of strain localization. Whereas alignment of the maximum compressive stress with bedding would inhibit the development of compaction localization (and thus promote distributed cataclastic flow), diffuse shear or compaction bands readily developed in Rothbach sandstone samples with σ_1 applied oblique or perpendicular to bedding.

LOUIS et al. (2007b) recently suggested that a diffuse mode of compaction localization is promoted by grain-scale heterogeneity, as characterized by relatively broad distributions of CT-number and grain contact diameter. They compared the data for Berea sandstone samples (cored perpendicular to bedding) with those for Bentheim and Diemelstadt sandstones. Whereas Berea sandstone tends to develop diffuse shear or compaction bands (analogous to what we observed in Rothbach sandstone), Bentheim and Diemelstadt sandstones readily develop relatively thin and discrete compaction bands when deformed to failure under high confinement (BAUD et al., 2004). To further investigate this question, we analyzed the distributions of CT-number (grey level) and grain contact length of an undeformed Rothbach sandstone sample. In Figure 12a, normalized grey level distributions of X-ray images acquired in Bentheim, Diemelstadt and Rothbach sandstones are represented. The distribution for the Rothbach sandstone was obtained by selecting in the original image higher porosity zones where compaction was observed to preferentially occur. In the same manner as for Berea sandstone (LOUIS et al., 2007b), the distribution for the Rothbach sandstone is significantly broader than for Bentheim and Diemelstadt sandstones, and therefore more heterogeneous. In Figure 12b, intergranular contacts were traced from optical microscope images, then measured in length with the automated function provided in ImageJ freeware. Apart from differences in average contact length, which varies with grain size, composition and degree of cementation, one can again clearly distinguish Bentheim and Diemelstadt sandstones with nearly identical narrow contact length distribution, from the Rothbach sandstone which shows significantly broader distribution. As proxies for grain-scale heterogeneity, these statistics of CT-number and grain contact length strongly support the idea that discrete compaction bands are promoted in a relatively homogeneous granular material, in agreement with recent numerical simulations using network (KATSMAN et al., 2005) and discrete element (WANG et al., 2008) models.
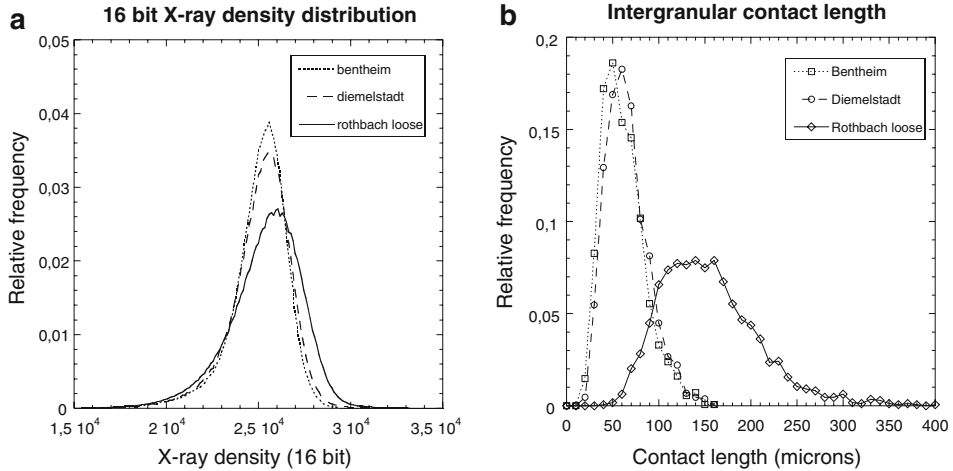
Figure 12

a. Grey level distribution of X-ray CT images from Bentheim, Diemelstadt and Rothbach sandstones. The distribution of the Rothbach is noticeably more spread than for the two other sandstones. b. Distribution of the intergranular contact length for Bentheim, Diemelstadt and Rothbach sandstones. As in a, the Rothbach sandstone is significantly different from the two others with larger intergranular contact length and broader distribution.

4.2. Compactive Yield Caps and Inelastic Deformation

BAUD *et al.* (2006) fitted the yield envelopes of four sandstones of porosity ranging from 13% to 23% with an elliptical cap of the form:

$$\frac{(P - C)^2}{A^2} + \frac{Q^2}{B^2} = 1$$

in which the ellipse is anchored at P* (A + C = P*) and B/A represents the aspect ratio of the cap. For Bentheim, Berea and Darley Dale cored perpendicular to bedding as well as Adamswiller cored parallel to bedding, they consistently found B/A > 1. Figure 13 shows that such elliptical caps provide a decent fit of our yield envelopes for Rothbach sandstone cored in the three studied orientations. The caps for the parallel and oblique orientations have comparable aspect ratios slightly smaller than 1 (Figs. 13a and 13b). The cap for the samples cored perpendicular to bedding has a significantly different shape with an aspect ratio of 1.27 (Fig. 13c) in the range of the values found by BAUD *et al.* (2006) for other sandstones.

Figures 13a-c also present contours in the stress space corresponding to specific values of the volumetric strain. Since in a sandstone plastic deformation of the solid grains is negligible at room temperature under the pressure conditions, in our experiments, the plastic porosity change $\Delta\phi^p$ represent the bulk of the plastic volumetric strain and to the first approximation we can take $\varepsilon_v^p = \Delta\phi^p$. Because a lot of our experiments were stopped after a few percents of axial strain for microstructural studies, we could only draw those contours over a relatively modest range of plastic volumetric
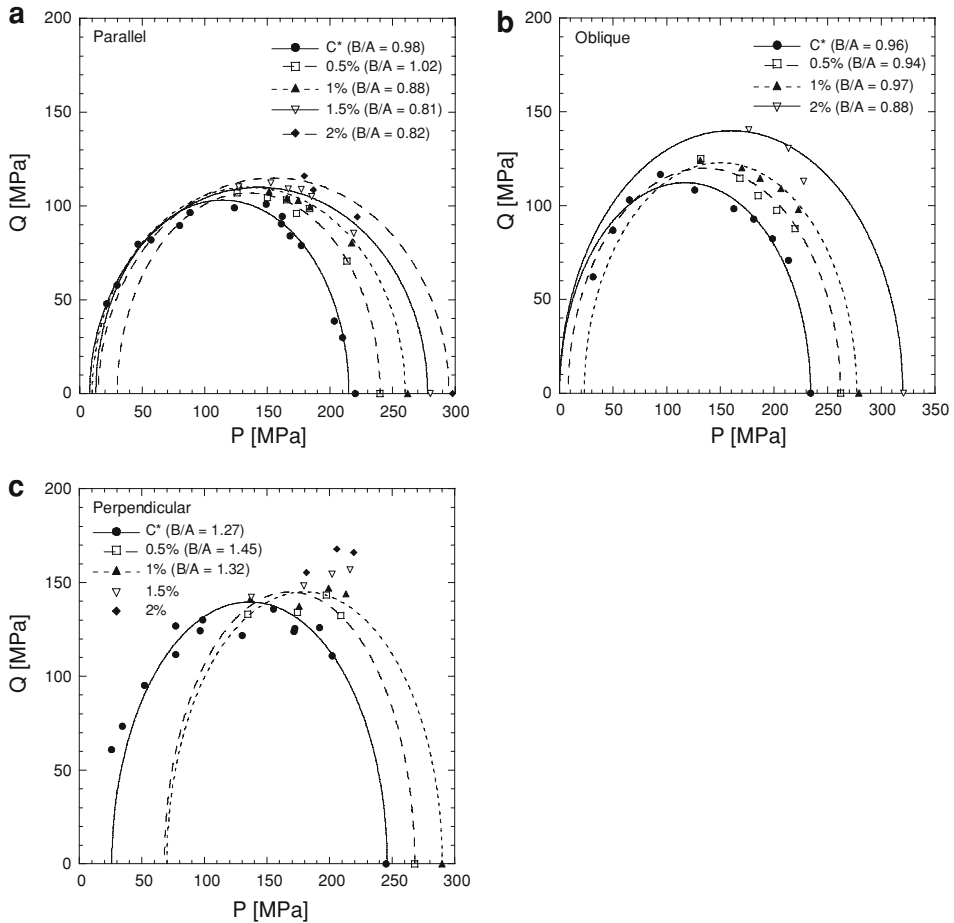
Figure 13
Yield envelopes, (Q, P) values at specific volumetric strains (0.5%, 1%, 1.5%, 2%) and corresponding elliptical fits for samples parallel (a), oblique (b) and perpendicular (c) to the bedding.

strain. Despite this limitation, Figures 13a-c show two important features: First, the shape of the contours varies significantly with increasing plastic strain for the three orientations. Our set of data on Rothbach sandstone presents therefore an overall poor agreement with both CAROLL's (1991) critical state model and the DIMAGGIO SANDLER (1971) cap model, which assumed a constant width and constant aspect ratio of the cap, respectively (BAUD *et al.*, 2006). The main observation of a cap aspect ratio significantly larger for the perpendicular samples is however still valid as plastic volumetric strain increased (Fig. 13c). Second, more strain hardening is observed for perpendicular and oblique samples than for parallel samples and therefore, since 0° (i.e., parallel) to bedding is the weakest orientation, the mechanical anisotropy quantified at the yield stress remains important as plastic volumetric strain increases.
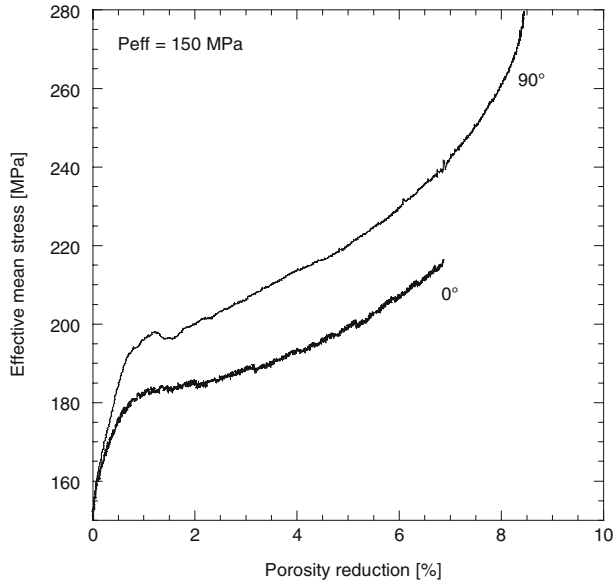
Figure 14

Effective mean stress P vs. porosity reduction for triaxial experiments at $P_{\text{eff}} = 150$ MPa on samples parallel and perpendicular to the bedding.

Figure 14 presents two experiments performed at 150 MPa of effective pressure to large levels of strain for parallel and perpendicular samples. Indeed, after 5% of plastic volumetric strain ($\sim 10\%$ axial strain), the gap between the two extreme orientations remains approximately the same at this pressure. We have seen in the previous sections that compaction localization is the dominant feature of compaction in oblique and perpendicular samples. Our data suggest that from a macroscopic point of view, the porosity reduction is comparable whether compactive shear bands, compaction bands or homogeneous cataclastic flow develop.

Because we wanted to compare the post-yield behavior against the critical state and cap models aforementioned, we assumed as a first-order approximation an elliptical yield cap for the three directions investigated, as if each of them were to reflect the behavior of a distinct isotropic material. The anisotropy of the Rothbach sandstone should be accounted for with a unique anisotropic model allowing for delineating three distinct yield envelopes for the same material. Such investigation is the objective of a future study.

5. Summary and Conclusion

The aim of this study was to investigate further the influence of sedimentary lamination in Rothbach sandstone on the anisotropy of yield stress and failure mode at

various effective pressures from 5 MPa to 250 MPa. The deformed samples were cored perpendicular, oblique (45 degrees) and parallel to the bedding. For both brittle strength and compactive yield stress, we measured for each effective pressure, maximum, intermediate and minimum values for perpendicular, oblique and parallel samples, respectively. These results could not be accounted for with the conceptual model of a layered medium for that the samples cored parallel to the bedding should have been mechanically stronger than the ones cored perpendicular to the bedding. Instead, the observed mechanical anisotropy was found consistent with the preferential orientation of the intergranular contacts subparallel to the bedding, according to the principle that an increase of the total contact surface alleviates stress on each individual contact, and therefore provides more strength to the overall structure.

At low effective pressure (5 MPa to 30 MPa), shear bands were observed to develop for all sample orientations investigated. In the shear enhanced compaction domain, AE activity and distribution of damage showed that compaction localization had occurred in perpendicular and oblique samples, while parallel samples had undergone more homogeneously distributed compaction. In perpendicular and oblique samples, compaction preferentially took place in relatively more porous and presumably weaker zones. Within these zones, localization was diffuse, which was accounted for by significant grain scale heterogeneity that prevented discrete compaction bands from propagating across the sample.

Analysis of the yield loci and post-failure deformation showed that elliptical envelopes provided a reasonable fit with our experimental data, and that mechanical anisotropy persisted through compaction, with comparable amounts of porosity reduction for the extreme directions investigated. A future study will be dedicated to improving the approach on anisotropic yield by using a simple methodology such as the one described by ODA (1993).

In conclusion, the mechanical anisotropy and failure modes of the Rothbach sandstone, which was studied for its characteristic layered structure, were found to be only partly controlled by it. In experiments where samples failed by shear-enhanced compaction, the macroscopic heterogeneity materialized by the layering certainly played a role in that, when favorably oriented with respect to the maximum compressive stress, higher porosity zones were preferentially compacted (diffuse compaction bands in perpendicular samples and diffuse compactive shear bands in oblique samples). However, compaction localization as indicated by AE signatures and punctual stress drops, may rather be related to grain scale mechanical heterogeneity within these zones, as attested by X-ray CT image and thin section analyses. As far as the mechanical anisotropy is concerned, we inferred from statistics on the preferred orientation of intergranular contacts that these features were likely responsible for the maximum, intermediate and minimum mechanical strength in samples cored perpendicular, oblique and parallel to the bedding, respectively. The development of a more realistic micromechanics model relating our macroscopic and microstructural observations should aim in particular at explaining how the same microstructural features

may impact in a similar way the anisotropy of brittle strength and compactive yield stress.

Acknowledgements

References

BAUD, P., KLEIN, E., and WONG, T.-F. (2004), *Compaction localization in porous sandstones: spatial evolution of damage and acoustic emission activity*, J. Struct. Geol. 26 (4), 603–624.

BAUD, P., LOUIS, L., DAVID, C., RAWLING, G.C., and WONG, T.-f. (2005), *Effects of bedding and foliation on mechanical anisotropy, damage evolution and failure mode*, Geol. Soc. London Special Publ. 245, 223–249.

BAUD, P., VAJDOVA, V., and WONG, T.-F. (2006), *Shear-enhanced compaction and strain localization: Inelastic deformation and constitutive modeling of four porous sandstones*, J. Geophys. Res. 111 (B12), doi: 10.1029/2005JB004101.

BÉSUELLE, P., BAUD, P., and WONG, T.-F. (2003), *Failure mode and spatial distribution of damage in Rothbach sandstone in the brittle-ductile transition*, Pure Appl. Geophys. 160 (5–6), 851–868.

BÉSUELLE, P., DESRUES, J., and RAYNAUD, S. (2000), *Experimental characterization of the localisation phenomenon inside a Vosges sandstone in a triaxial cell*, Int. J. Rock Mech. 37, 1223–1237.

CARROLL, M. M. (1991), *A critical state plasticity theory for porous reservoir rock*, Recent Adv. Mechan. Struct. Continua 117.

DAVID, C., WONG, T.-F., ZHU, W., and ZHANG, J. (1994), *Laboratory measurement of compaction induced permeability change in porous rocks: Implication for the generation and maintenance of pore pressure excess in the crust*, Pure Appl. Geophys. 143, 425–456.

DESRUES, J., CHAMBON, R., MOKNI, M., and MAZEROLLE, F. (1996), *Void ratio evolution inside shear bands in triaxial sand specimens studied by computed tomography*, Geotechnique 46 (3), 529–546.

DIMAGGIO, F. L. and SANDLER, I. S. (1971), *Material model for granular soils*, J. Eng. Mech. Div. Am. Soc. Civ. Eng. 97, 935–950.

HULL, D., *An Introduction to Composite Materials* (Cambridge University Press, Cambridge 1981).

JAEGER J. C., *Fundamentals of Rock Mechanics* (Chapman and Hall, London 1979).

KATSMAN, R., AHARONOV, E., and SCHER, H. (2005), *Numerical simulation of compaction bands in high-porosity sedimentary rock*, Mechan. Mat. 37, 143–162.

KETCHAM, R. A. and CARLSON, W. D. (2001), *Acquisition, optimization and interpretation of X-ray computed tomographic imagery: Applications to the geosciences*, Comp. and Geosci. 27 (4), 381–400.

KETCHAM, R. A. and ITURRINO, G. J. (2005), *Nondestructive high-resolution visualization and measurement of anisotropic effective porosity in complex lithologies using high-resolution X-ray computed tomography*, J. Hydrol. 302 (1-4), 92–106.

LOUIS, L., WONG, T.-f., and BAUD, P. (2007a), *Imaging strain localization by X-ray radiography and digital image correlation: Deformation bands in Rothbach sandstone*, J. Struct. Geol. 29 (1), 129–140.

LOUIS, L., BAUD, P., and WONG, T.-f. (2007b), *Characterization of pore-space heterogeneity in sandstone by X-ray computed tomography*, Geol. Soc. London Special Publ. 284, 127–146.

LOUIS, L., DAVID, C., METZ, V., ROBION, P., MENENDEZ, B., and KISSEL, C. (2005), *Microstructural control on the anisotropy of elastic and transport properties in undeformed sandstones*, Int. J. Rock Mech. 42 (7–8), 911–923.

MENENDEZ, B., ZHU, W. L., and WONG, T. F. (1996), *Micromechanics of brittle faulting and cataclastic flow in Berea sandstone*, J. Struct. Geol. *18* (1), 1–16.

MILLIEN, A., *Comportement anisotrope du grès des Vosges: élasto-plasticité, localisation, rupture* (Ph.D. Thesis, Université Joseph Fourier - Grenoble I, Grenoble 1992).

ODA, M. (1993), *Inherent and induced anisotropy in plasticity theory of granular soils*, Mechan. Mater. *16* (1–2), 35–45.

RAWLING, G. C., BAUD, P., and WONG, T.-F. (2002), *Dilatancy, brittle strength, and anisotropy of foliated rocks: Experimental deformation and micromechanical modeling*, J. Geophys. Res.-Sol. Earth *107* (B10), ETG 8-1.

UNDERWOOD, E. E., *Quantitative Stereology* (Addison-Wesley, MA, 1970).

VINEGAR, H. J., DE WAAL, J. A., and WELLINGTOM, S. L. (1991), *CT studies of brittle failure in castlegate sandstone*, Int. J. Rock Mech. *28* (5), 441–448.

WALSH, J. B. and BRACE, W.F. (1964), *A fracture criterion for brittle anisotropic rock*, J. Geophys. Res. *69* (3), 449–456.

WANG, B., CHEN, Y., and WONG, T.-F. (2008), *A discrete element model for the development of compaction localization in granular rock*, J. Geophys. Res. *113*, doi:10.1029/2006JB004501.

WONG, T.-f., DAVID, C., and ZHU, W. (1997), *The transition from brittle faulting to cataclastic flow in porous sandstones : Mechanical deformation*, J. Geophys. Res. *102*, 3009–3025.

WONG, T.-f. and WU, L. C. (1995), *Tensile stress concentration and compressive failure in cemented granular material*, Geophys. Res. Lett. *22*, 1649–1652.

ZHANG, J., WONG, T.-F., and DAVIS, D. M. (1990), *Micromechanics of pressure-induced grain crushingin porous rocks*, J. Geophys. Res. *95*, 341–352.

ZHU, W. and WONG, T.-F. (1997), *The transition from brittle faulting to cataclastic flow in porous sandstones: Permeability evolution*, J. Geophys. Res. *102*, 3027–3041.

To access this journal online:
www.birkhauser.ch/pageoph